Research Square

Preprints are preliminary reports that have not undergone peer review.
They should not be considered conclusive, used to inform clinical practice,
or referenced by the media as validated information.

Diagnostic-Anchored Neural State-Space Modeling of Electrochemical Degradation and Load-Dependent Voltage Loss in Proton Exchange Membrane Fuel Cells

Jiayan Xia
Yangtze University
Xinru Yang
Yangtze University
Chengyang Wei
Yangtze University
Wenjuan He
Yangtze University
Chenxi Yu
Yangtze University
Yongqian Zhou
zhouyq@yangtzeu.edu.cn
Yangtze University

Article

Keywords: Proton exchange membrane fuel cell, Cathode degradation, Electrochemical characterization, Neural state-space model, Accelerated stress testing, Load-dependent voltage loss

Posted Date: November 23rd, 2026

DOI: https://doi.org/10.21203/rs.3.rs-11609038/v1

License: This work is licensed under a Creative Commons Attribution 4.0 International License.
Read Full License

Additional Declarations: No competing interests reported.

Diagnostic-Anchored Neural State-Space Modeling of Electrochemical Degradation and Load-Dependent Voltage Loss in Proton Exchange Membrane Fuel Cells

Manuscript type: Research Article

Jiayan Xia[a,b], Xinru Yang[a,b], Chengyang Wei[b], Wenjuan He[b], Chenxi Yu[b] Yongqian Zhou[a,b] *

[a] School of Electronic Information and Electrical Engineering, Yangtze University, Jingzhou 434022, Hubei, China
[b] National Demonstration Center for Experimental Electrical and Electronic Education, Yangtze University, Jingzhou 434022, Hubei, China

Author e-mail addresses

Author	E-mail address
Jiayan Xia	2135037676@qq.com
Xinru Yang	1175057900@qq.com
Chengyang Wei	1489541653@qq.com
Wenjuan He	19312752156@163.com
Chenxi Yu	2787209115@qq.com
Yongqian Zhou	zhouyq@yangtzeu.edu.cn

Keywords

Proton exchange membrane fuel cell; Cathode degradation; Electrochemical characterization; Neural state-space model; Accelerated stress testing; Load-dependent voltage loss

Funding

This work was supported by the National Natural Science Foundation of China [Grant number 62350410484].

CRediT authorship contribution statement

Jiayan Xia: Conceptualization, Software, Validation, Formal analysis, Investigation, Visualization, Writing - original draft.
Xinru Yang: Methodology, Validation, Software, Writing - review & editing.
Chengyang Wei: Validation, Visualization, Writing - original draft.
Wenjuan He: Investigation, Data curation, Formal analysis.
Chenxi Yu: Resources, Writing - review & editing.
Yongqian Zhou: Supervision, Funding acquisition, Resources, Project administration, Writing - review & editing.

Declaration of competing interest

The authors declare that they have no known competing financial interests or personal relationships that could have appeared to influence the work reported in this paper.

Data availability statement

The raw experimental data analyzed in this study are publicly available in the Figshare repository (https://doi.org/10.6084/m9.figshare.25450177). The processed datasets, physical-cell grouping information, and model prediction results generated in this study are available from the corresponding author upon reasonable request.

Code availability

The custom code used for data preprocessing, model development, training, and evaluation is available from the corresponding author upon reasonable request.

Declaration of generative AI and AI-assisted technologies in manuscript preparation

During the preparation of this work, the authors used ChatGPT (OpenAI) to assist with language editing, formatting, and improving clarity. After using this tool, the authors reviewed and edited the content as needed and take full responsibility for the content of the published article.

Diagnostic-Anchored Neural State-Space Modeling of Electrochemical Degradation and Load-Dependent Voltage Loss in Proton Exchange Membrane Fuel Cells

ABSTRACT

Understanding proton exchange membrane fuel cell (PEMFC) durability requires connecting electrochemical degradation to voltage loss under different operating loads. We develop a diagnostic-anchored neural state-space model that represents catalyst/interface, protonic/ionic, ohmic, and oxygen-transport responses through four evolving state coordinates. Material descriptors, accelerated-stress conditions, and beginning-of-test characterization condition state evolution. Diagnostic-specific observation masks enable learning from measurements acquired at different aging stages, while a load-structured decoder predicts voltage loss at five current densities. Using 37 curated aging trajectories, repeated cell-grouped fivefold cross-validation yielded a mean voltage-loss MAE of 12.34 mV across five loads and R^2 = 0.901 at 1.0 A cm^{-2}. The model reconstructed electrochemically active surface area loss with R^2 = 0.809. Replacing the structured decoder increased mean voltage-loss MAE to 15.50 mV. Across 13 nominally matched comparisons, raising the upper potential limit from 0.95 to 1.15 V was associated with median increases of 0.294 in active-area-loss fraction and 0.159 V in voltage loss at 1.0 A cm^{-2}. This framework unifies electrochemical diagnostic reconstruction and load-dependent performance prediction for comparative cathode durability assessment within the investigated accelerated-stress conditions.

1. Introduction

Decarbonizing transport and distributed power requires conversion technologies that combine low emissions with reliable operation. The International Energy Agency identifies a large gap between global hydrogen use and low-emissions production[1]. The European Union has established hydrogen-refueling infrastructure requirements for 2030[2], and the U.S. Department of Energy continues to prioritize fuel-cell durability, performance, and cost[3]. Research on catalysts for methanol steam reforming also reflects efforts to diversify hydrogen supply pathways[4]. Proton exchange membrane fuel cells (PEMFCs) offer rapid response and high power density, making them attractive for mobile and flexible power applications. Their wider use depends on sustaining performance under demanding duty cycles. Cullen et al. identified durability challenges for heavy-duty vehicles[5], while Mora et al. examined the influence of operating temperature on cathode aging and oxygen transport[6].

PEMFC voltage decline reflects the combined evolution of several electrochemical processes. El-Kharouf et al. reviewed fuel-cell degradation and durability-testing methods[7], while Borup et al. described interactions among catalyst, support, membrane, and interfacial deterioration[8]. Laghryb et al. connected cathode catalyst degradation mechanisms with characterization and modeling techniques[9]. Coats and Pylypenko examined catalyst-layer damage under idle and load cycling[10], and Lim et al. investigated a cathode design intended to mitigate corrosion-related deterioration[11]. These changes affect active surface area, proton conduction, ohmic resistance, and oxygen transport through different pathways. Their voltage signatures can overlap, leaving cell voltage insufficient to distinguish the internal changes associated with performance loss.

Electrochemical diagnostics provide complementary measurements of these responses. Schneider et al. showed how ionomer-to-carbon ratio and relative humidity affect cathode aging[12], and Pedram et al. related these conditions to microstructural changes using quantitative microscopy[13]. Zheng et al. developed a method to diagnose catalyst-layer ionomer degradation[14], while Jeong et al. investigated chemical degradation of electrode ionomer[15]. Raab and Weber analyzed aging through impedance measurements[16]; García-Salaberri et al. examined local oxygen-transport resistance[17], and Afra et al. measured oxygen concentration at the cathode catalyst-layer/membrane interface[18]. Aslam et al. used simultaneous thermal and visual imaging to characterize liquid water in fuel-cell channels[19]. The diagnostic quantities differ in physical sensitivity and are often collected at different aging stages. Schneider et al. released a dataset combining cathode formulations, accelerated stress conditions, repeated diagnostics, and polarization curves[20], providing a basis for analyzing these heterogeneous observations together.

Data-driven approaches have advanced fuel-cell degradation and performance prediction. Ma et al. incorporated electrochemically active surface area (ECSA) loss into stack degradation prediction[21]. Dong et al. introduced a voltage-integral

indicator for remaining-useful-life estimation[22], and Hua et al. proposed hybrid forecasting using dynamic aging indicators[23]. Quan et al. combined bidirectional recurrent learning and Transformer components under different currents[24]. Yu et al. developed an interpretable model for degradation and polarization-curve prediction[25], whereas Zhang et al. proposed multi-point prognostics across operating conditions[26]. Ke et al. integrated degradation-mechanism information with deep learning for dynamic load cycles[27]. These advances establish effective approaches for modeling temporal degradation and predicting electrical performance across operating conditions.

Physics-guided methods further link learning algorithms to electrochemical knowledge. Guo et al. developed an interpretable uncertainty-quantification framework[28], Ko et al. embedded degradation relations in a physics-informed neural network[29], and Wei et al. combined Crossformer learning with physical constraints[30]. Liu et al. coupled physics-informed prediction with conformal uncertainty assessment[31], while Zhu et al. integrated symbolic regression and physics-informed learning for long-term prognosis[32]. Mechanistic studies clarify the coupling between aging and load-dependent losses. Hao et al. modeled heterogeneous aging across electrochemical reaction and transport scales[33]; Goswami et al. examined reactive transport in degrading catalyst layers[34]; and Liu et al. linked carbon corrosion to nonlinear mass-transport deterioration[35]. Together, these studies motivate models that connect measured degradation responses with their electrical consequences.

A central challenge in comparative cathode durability assessment is to connect material- and stress-dependent aging, asynchronously measured electrochemical diagnostics, and voltage losses across operating loads within one dynamic model. ECSA, double-layer capacitance, catalyst-layer ionic resistance, high-frequency resistance, and oxygen-transport resistance probe different responses and may be measured at different aging stages. Their integration requires state variables linked to experimental diagnostics, observation masks for unavailable measurements, and dynamics capable of representing early activation and accumulated degradation. A load-dependent output model can then relate the evolving states to voltage loss at several operating currents. This framework is suited to comparative analysis of cathode formulations and accelerated stress protocols within a characterized experimental domain.

Here, we develop a diagnostic-anchored neural state-space model for PEMFC cathode durability assessment using 37 curated aging trajectories. Four evolving state coordinates represent catalyst/interface, protonic/ionic, ohmic, and oxygen-transport diagnostic groups. Material descriptors, accelerated-stress conditions, and beginning-of-test characterization condition state evolution, while measurement masks preserve the availability of ten diagnostic targets across nine planned aging stages. A structured decoder maps the states to voltage loss at five current densities and the corresponding power-density loss.

The contributions of this study are threefold.

(1) We establish a multi-diagnostic state representation anchored to experimentally measured quantities;

(2) We develop conditioned state transitions that describe accumulated catalyst degradation, transient activation, and signed diagnostic changes;

(3) We introduce a load-structured diagnostic-to-performance mapping evaluated through grouped cross-validation, matched-condition analysis, and component ablations.Together, the framework supports comparative electrochemical degradation assessment and load-dependent performance analysis under the investigated accelerated-testing conditions.

2. Experimental Dataset and Electrochemical Characterization

2.1. Dataset and accelerated durability protocol

This study uses the publicly available in-situ cathode degradation dataset reported by Schneider et al.[20] and deposited in Figshare[36]. The experimental campaign investigated the effects of cathode composition and accelerated-stress conditions on proton exchange membrane fuel cell (PEMFC) durability. The original archive contains 42 experimental labels covering different catalyst formulations, ionomer properties, electrode structures, and operating conditions. After resolving repeated experimental records, 37 distinct aging trajectories were retained for analysis.

The durability protocol combined voltage-cycling accelerated stress testing (AST) with repeated electrochemical characterization. Beginning-of-test (BoT) measurements included polarization curves, cyclic voltammetry (CV), linear sweep voltammetry (LSV), H_2/Air and H_2/N_2 electrochemical impedance spectroscopy (EIS), and limiting-current measurements.

Subsequent characterization was scheduled after 10, 100, 1000, 3000, 5000, 10,000, and 20,000 cycles, followed by end-of-test (EoT) measurements at 30,000 cycles. Together with BoT, these measurements define nine planned aging stages spanning initial conditioning and progressive performance deterioration.

2.2. Material and stress descriptors

The cathode formulations covered ionomer-to-carbon (I/C) ratios of 0.5, 0.8, and 1.2; ionomer equivalent weights of 720, 790, 830, and 980 g mol^{-1}; and Pt/C ratios ranging from 20% to 60%. Additional descriptors included measured platinum loading, catalyst chemistry, catalyst supplier, and carbon-support type. The principal stress variables were the upper potential limit (UPL), set to 0.95 or 1.15 V, and AST relative humidity, set to 40%, 70%, or 100%.

These descriptors define the material and stress context of each aging trajectory. Table 1 summarizes the model inputs, electrochemical measurements, and performance targets. Material and stress descriptors condition degradation-state evolution, whereas electrochemical diagnostics provide measured degradation responses.

Table 1. Experimental descriptors, electrochemical diagnostic measurements, and performance targets used in the degradation-state model.

Category	Variables or measurements	Role in the study
Material descriptors	Pt loading; I/C ratio; ionomer equivalent weight; Pt/C ratio; catalyst chemistry; supplier; carbon-support type	Material-dependent state evolution
Stress descriptors	UPL; AST relative humidity	Accelerated-aging context
Catalyst/interface diagnostics	ECSA; CV-derived Cdl; EIS-derived Cdl at 200 and 450 mV	Catalyst/interface state supervision
Protonic/ionic diagnostics	Rion at 200 and 450 mV	Protonic/ionic state supervision
Ohmic diagnostics	HFR at 200 and 450 mV	Ohmic state supervision
Oxygen-transport diagnostics	Pressure-dependent and pressure-independent oxygen-transport resistance	Mass-transport state supervision
BoT characterization	H_2 crossover current; available BoT diagnostics	Initial electrochemical context
Performance targets	Voltage loss at five current densities; derived power-density loss	Load-dependent performance assessment

2.3. Electrochemical measurements and diagnostic availability

Electrochemical measurements were organized according to their principal sensitivity to catalyst/interface, protonic/ionic, ohmic, and oxygen-transport responses. CV provided electrochemically active surface area (ECSA) and double-layer capacitance (Cdl). H_2/N_2 EIS supplied catalyst-layer ionic resistance (Rion), high-frequency resistance (HFR), and EIS-derived Cdl at 200 and 450 mV. Limiting-current measurements provided pressure-dependent and pressure-independent oxygen-transport resistance. Polarization curves characterized the cell voltage response over the measured current-density range, while H_2 crossover current obtained from LSV was retained as part of the BoT characterization.

Diagnostic availability varied across aging stages. CV, EIS, and polarization measurements were collected at multiple stages, whereas oxygen-transport measurements were concentrated near BoT and EoT. Each diagnostic was therefore associated with a binary availability mask identifying whether a valid measurement existed at a given stage. These masks were used during training to calculate reconstruction errors only from observed diagnostic targets, preserving the original measurement schedule.

2.4. Experimental-trajectory organization and preprocessing

The experimental records were organized according to their resolved measurement trajectories. The curated dataset contained 37 trajectories aligned to the nine planned aging stages, producing 333 trajectory–stage entries. This structure defines the aging-stage grid; individual diagnostics retain their actual observation availability.

To evaluate generalization across experimental trajectories, all observations sharing a resolved physical-cell grouping were assigned to the same cross-validation partition. Numerical material and stress descriptors were median-imputed and standardized using training-partition statistics. Categorical descriptors were one-hot encoded, with unseen categories handled without accessing test-partition information. BoT diagnostic inputs followed the same training-only preprocessing procedure, and availability indicators distinguished observed measurements from imputed inputs. Missing diagnostic supervision targets remained unobserved throughout model training.

2.5. Construction of diagnostic degradation targets

Diagnostic degradation was defined relative to each trajectory's BoT measurements to separate aging-related changes from initial performance differences. ECSA degradation was expressed as fractional active-area loss, while the remaining diagnostic responses were represented by signed absolute changes:

$$d_{ECSA}(t) = \frac{ECSA_0 - ECSA_t}{ECSA_0} \qquad (1)$$
$$\Delta x_t = x_t - x_0$$

Here, k denotes the aging stage, and x represents a diagnostic quantity other than ECSA. The fractional ECSA-loss definition retains negative values associated with early active-area increases, while signed changes preserve the direction of resistance and capacitance evolution.

Ten diagnostic targets were constructed: ECSA loss; CV-derived Cdl change; EIS-derived Cdl changes at 200 and 450 mV; Rion changes at both potentials; HFR changes at both potentials; and changes in the pressure-dependent and pressure-independent oxygen-transport resistances. These measurements were assigned to four diagnostic groups, providing the observation targets for the corresponding state coordinates described in Section 3.

2.6. Load-dependent performance targets and aging coordinate

Electrical performance degradation was evaluated using polarization curves measured at 100% relative humidity. Voltage loss at current density j and aging stage k was defined relative to the corresponding BoT voltage. Power-density loss was obtained directly from the voltage difference:

$$\Delta V(j,t) = V(j,0) - V(j,t) \qquad (2)$$
$$\Delta P(j,t) = j\Delta V(j,t)$$

Voltage-loss targets were evaluated at current densities of 0.1, 0.5, 1.0, 1.5, and 2.0 A cm^{-2}. Voltages at these fixed currents were obtained by interpolation within the available polarization-curve range, without extrapolation. Power-density loss was calculated from the measured or predicted voltage loss and required no separate prediction model.

The nonuniform spacing of the AST stages was represented using a normalized logarithmic aging coordinate, ranging from zero at BoT to one at 30,000 cycles. Its mathematical definition and use in the state transitions are presented in Section 3. Figure 1 summarizes the experimental conditions, diagnostic measurements, target construction, and subsequent diagnostic-to-performance modeling workflow.

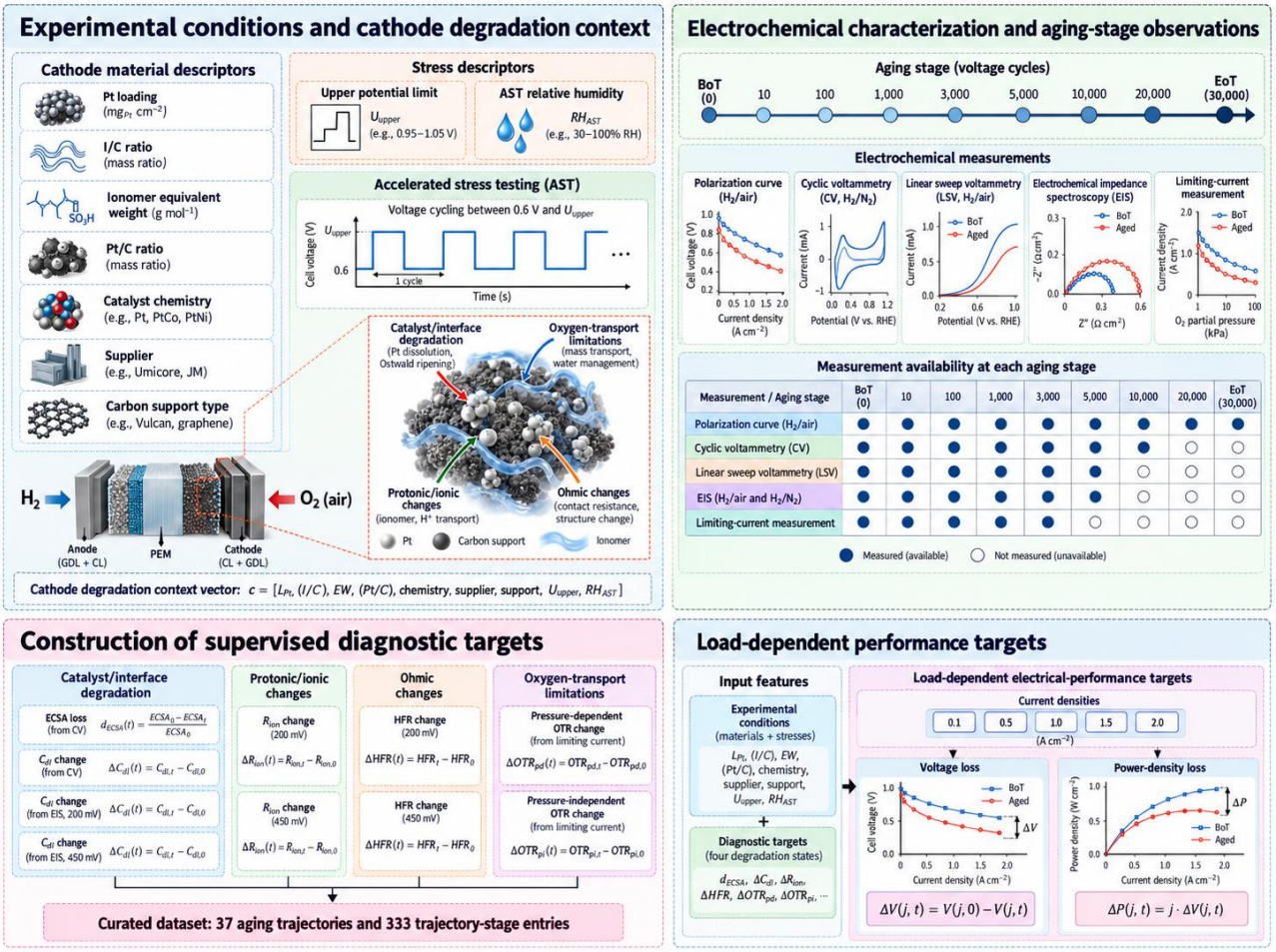


Figure 1. Experimental-to-computational workflow for diagnostic-anchored PEMFC degradation analysis. (a) Experimental conditions and principal cathode degradation processes. (b) Electrochemical characterization, aging-stage observations, and diagnostic availability. (c) Organization of measured diagnostic changes into four supervised degradation-state groups. (d) Mapping of degradation states to load-dependent voltage and power-density losses. Diagnostic availability masks distinguish recorded measurements from unobserved targets.

3. Diagnostic-Anchored Neural State-Space Framework

3.1. Problem formulation and framework overview

The proposed framework links material- and stress-dependent degradation to electrochemical diagnostic responses and load-dependent voltage loss. The framework is hereafter referred to as the electrochemically constrained multi-pathway neural state-space model (EC-MP-NSSM). Each experimental trajectory is characterized by a static context vector c, containing cathode material descriptors, accelerated-stress conditions, and beginning-of-test (BoT) measurements. Its evolution is represented by a four-dimensional latent state vector z_k, whose coordinates correspond to catalyst/interface (cat), protonic/ionic (ion), ohmic (ohm), and mass-transport (mt) responses.

The model consists of three connected components. A context-conditioned state-transition module describes degradation across aging stages. Pathway-specific observation functions reconstruct the corresponding electrochemical diagnostics, providing direct supervision of the latent states. A load-structured decoder maps these states to voltage loss at five current densities. Figure 2 illustrates the resulting architecture and the relationships among state evolution, diagnostic observations, and electrical performance.

The experimental stages are unevenly spaced in cycle number. A normalized logarithmic aging coordinate represents this progression:

$$t_k = \frac{\ln(1+N_k)}{\ln(1+N_{\max})}, \quad N_{\max} = 30000 \tag{3}$$

Here, N_k denotes the accumulated AST cycles at stage k. The coordinate increases from zero at BoT to one at end-of-test (EoT). The interval $\Delta t_k = t_k - t_{k-1}$ determines the step size of state evolution.

3.2. Material- and stress-conditioned state evolution

The four state coordinates follow transition rules matched to their diagnostic responses. All coordinates are initialized at zero because the degradation targets are defined relative to BoT. The catalyst/interface state represents accumulated degradation through non-negative increments:

$$z_{cat,k} = z_{cat,k-1} + \Delta t_k \mathrm{softplus}\left[f_{cat}(z_{k-1}, c, t_k)\right] \tag{4}$$

The protonic/ionic, ohmic, and mass-transport states permit signed changes:

$$z_{q,k} = z_{q,k-1} + \Delta t_k \tanh\left[f_q(z_{k-1}, c, t_k)\right], \quad q \in \{ion, ohm, mt\} \tag{5}$$

Each transition function is implemented using a multilayer perceptron. The input features include the preceding state, material and stress context, normalized aging coordinate, squared and square-root aging features, and the current aging interval. The non-negative catalyst transition describes accumulated deterioration, while signed transitions accommodate increases and decreases in resistance- and transport-related diagnostic responses.

Early catalyst behavior is represented by a transient activation term:

$$A_k = A_0\left[1 - \exp\left(-\frac{t_k}{\tau_r}\right)\right]\exp\left(-\frac{t_k}{\tau_d}\right) \tag{6}$$

The parameter A_0 controls activation amplitude, while τr and τd determine its rise and decay. The transient response is zero at BoT, develops during early aging, and diminishes at later stages. Combined with accumulated catalyst degradation, it enables the model to represent early ECSA increases and subsequent active-area loss within a common trajectory.

3.3. Diagnostic anchoring and observation model

Diagnostic anchoring assigns each latent state coordinate to a defined group of electrochemical measurements. The catalyst/interface state is supervised by ECSA loss and changes in CV- and EIS-derived double-layer capacitance. The protonic/ionic and ohmic states are linked to ionic resistance and high-frequency resistance at 200 and 450 mV, respectively. The mass-transport state is supervised by pressure-dependent and pressure-independent oxygen-transport resistance.

Each observation function receives only the latent coordinate associated with its diagnostic group. ECSA reconstruction additionally incorporates transient activation:

$$d_{ECSA,k} = z_{cat,k} - A_k$$
$$d_{m,k} = h_m\left(z_{p(m),k}\right), \quad m \neq ECSA \tag{7}$$

Here, $d_{m,k}$ denotes the reconstructed degradation response of diagnostic target m at aging stage k, h_m represents the corresponding observation function, and p(m) identifies the degradation-state coordinate associated with target m. All diagnostic targets are defined relative to their beginning-of-test (BoT) measurements, as described in Section 2.5.

The experimental diagnostics have different measurement frequencies and aging-stage coverage. A binary observation mask identifies the availability of each target, ensuring that reconstruction losses are calculated only from valid measurements. Diagnostic errors are normalized separately for each target before aggregation to account for differences in physical units and numerical scales. This observation-based supervision enables the model to integrate asynchronously acquired electrochemical measurements and learn a unified degradation-state representation that remains linked to experimentally defined diagnostic responses.

3.4. Load-structured voltage decoder

The voltage decoder connects evolving diagnostic states to their electrical consequences. Predicted voltage loss at aging stage

k and current density j is expressed as the sum of four explicit pathway contributions and a recurrent residual correction:

$$\Delta V(k,j) = V_{cat}(k,j) + V_{ion}(k,j) + V_{ohm}(k,j) + V_{mt}(k,j) + V_{res}(k,j) \quad (8)$$

Each explicit contribution combines its corresponding state coordinate with a learnable context-dependent gain and a pathway-specific current-response function. The current-response functions are defined as follows:

$$b_r(j) = \begin{cases} j^p, r = cat \\ j, r = ion \\ j, r = ohm \\ \dfrac{-\ln\left(1-\frac{j}{j_{\lim}}\right)}{-\ln\left(1-\frac{j_{ref}}{j_{\lim}}\right)}, r = mt \end{cases} \quad (9)$$

Here, p is the learned catalyst-response exponent, jlim is the learned limiting-current scale, and jref is the reference current density used to normalize the transport response. The catalyst term follows a power-law dependence, the ionic and ohmic terms vary linearly with current density, and the transport term increases nonlinearly toward the limiting-current scale.

Material- and stress-conditioned gains adjust the explicit contributions for each trajectory. Catalyst and transport gains are constrained to be positive, while ionic and ohmic gains permit signed responses. The recurrent residual accounts for voltage-loss behavior not captured by the explicit pathways and is regularized during training. The resulting decomposition provides load-dependent model-attributed contributions while retaining a separate residual term.

Predicted power-density loss is calculated directly from voltage loss using Eq. (2), without a separate prediction network.

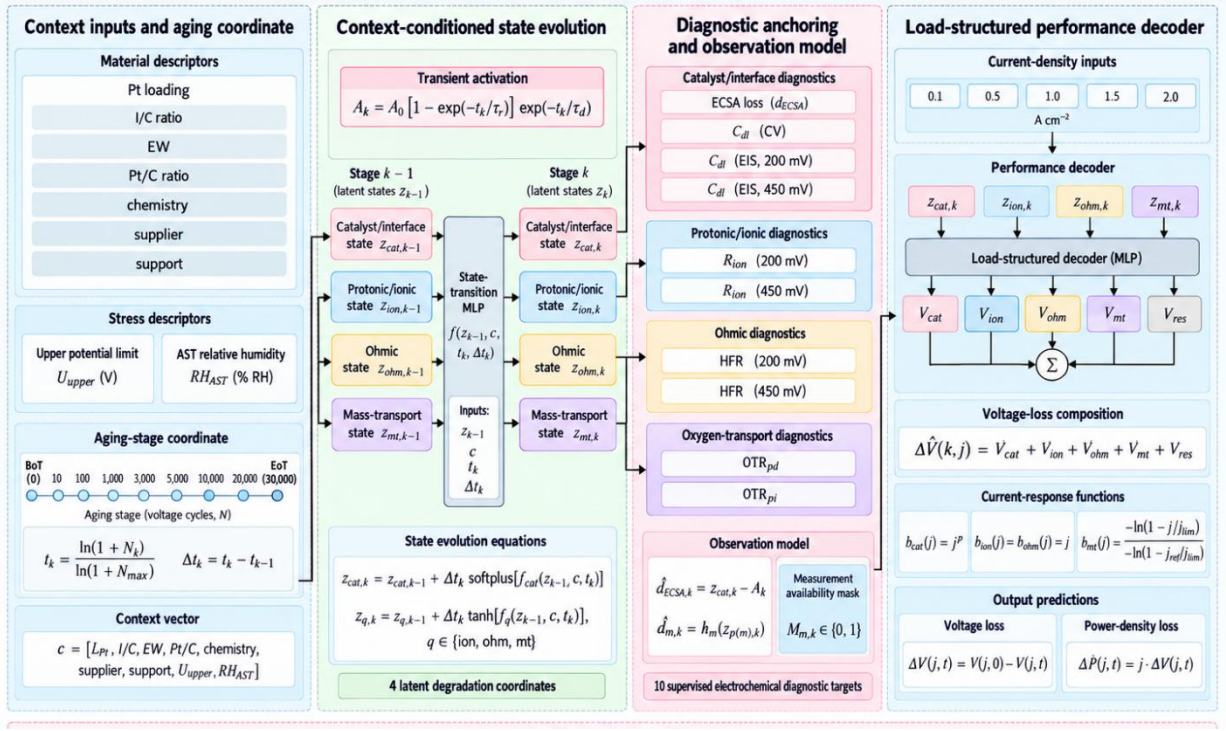


Figure 2. Architecture of the diagnostic-anchored neural state-space model.

3.5. Electrochemical constraints and learning objective

The learning objective combines diagnostic reconstruction and voltage prediction with constraints derived from the experimental degradation behavior. The catalyst branch separates accumulated degradation from transient activation, allowing early ECSA recovery while favoring nondecreasing ECSA loss after 1000 cycles through a soft monotonicity penalty. Weak second-difference penalties regulate the ionic, ohmic, and mass-transport trajectories without enforcing monotonic evolution.

Matched upper-potential-limit (UPL) conditions provide an additional stress-related constraint. Within each training partition, trajectories tested at 0.95 and 1.15 V are paired when their nominal cathode formulations and other stress descriptors match. The ordering penalty favors greater EoT ECSA loss, catalyst-state degradation, and voltage loss at 1.0 A cm^{-2} under the higher UPL. An endpoint-ranking penalty further regulates the relative severity of predicted degradation across trajectories.

The total training objective is

$$\mathcal{L} = 0.70\mathcal{L}_{\text{state}} + 2.00\mathcal{L}_{\text{voltage}} + 0.10\mathcal{L}_{\text{ECSA}} + 0.10\mathcal{L}_{\text{UPL}} + 0.005\mathcal{L}_{\text{smooth}} + 0.035\mathcal{L}_{\text{rank}} + 0.002\mathcal{L}_{\text{res}} \quad (10)$$

The state and voltage terms use target-wise robust losses combining Huber error with a small squared-error component. Diagnostic targets are scaled individually using training-partition statistics, whereas a common scale is applied across the five voltage-loss targets. The remaining terms correspond to late-stage ECSA consistency, matched-UPL ordering, state-trajectory smoothness, endpoint ranking, and residual regularization. This objective jointly optimizes electrochemical diagnostic fidelity and load-dependent voltage prediction.

3.6. Model optimization and implementation

Model optimization consists of two stages. First, the context-conditioned transitions, diagnostic observation functions, and voltage decoder are trained jointly using Eq. (10). Complete aging trajectories are processed within each training partition. AdamW optimization uses an initial learning rate of 1.5×10^{-3}, weight decay of 8×10^{-5}, and gradient clipping at 4.0. Training runs for a maximum of 1100 epochs, with early stopping based on internal validation after at least 140 epochs. A learning-rate scheduler reduces the learning rate when validation improvement stalls.

In the second stage, the trained state-transition and diagnostic-observation modules are frozen, and the voltage decoder is refined for up to 140 epochs at a learning rate of 6×10^{-4}. This stage adjusts the electrical mapping while preserving the learned diagnostic-state representation.

The framework is implemented in PyTorch. Numerical preprocessing and conventional machine-learning baselines use standard Python scientific-computing libraries. Random seeds are fixed, and deterministic operations are enabled where supported. Table 2 summarizes the architecture, optimization, and validation settings.

Table 2. Principal architecture, optimization, and validation settings of the diagnostic-anchored neural state-space model.

Item	Setting
Latent degradation coordinates	4
Hidden dimension	72
Dropout rate	0.07
Optimizer	AdamW
Initial learning rate	1.5×10^{-3}
Weight decay	8×10^{-5}
Maximum training epochs	1100
Minimum epochs before early stopping	140
Early-stopping patience	130 epochs
Gradient-clipping threshold	4.0
Voltage fine-tuning	Up to 140 epochs
Fine-tuning learning rate	6×10^{-4}
Outer validation	Repeated fivefold, grouped by physical-cell identity
Repeated split seeds	142, 152, 162
Inner validation fraction	Approximately 18%

3.7. Grouped validation, baselines, and ablation design

Generalization is evaluated using three repetitions of fivefold cross-validation grouped by resolved physical-cell identity. All

aging stages belonging to the same group remain within one outer fold. Preprocessing statistics, parameter optimization, early stopping, and model selection use only the outer-training data. Approximately 18% of the outer-training groups are assigned to internal validation, with UPL-stratified sampling when feasible. After selecting the training duration, the model is reinitialized and fitted on the complete outer-training partition before prediction on held-out groups.

The proposed framework is compared with conventional regression, sequence-learning models, and an unconstrained neural state-space model. The reported regression baselines comprise Random Forest and Extra Trees. The reported temporal baselines comprise GRU, LSTM, temporal convolutional network, Transformer, and Transformer–GRU. The unconstrained state-space baseline uses ten latent coordinates. All models follow the same outer grouped-validation protocol.

Targeted ablations evaluate the effects of material and stress conditioning, the structured voltage decoder, recurrent residual correction, transient catalyst activation, combined electrochemical penalties, the UPL-ordering constraint considered separately, and the explicit mass-transport voltage contribution. Model performance is assessed using mean absolute error (MAE), root-mean-square error (RMSE), coefficient of determination (R^2), and Spearman rank correlation. Normalized RMSE is additionally used to compare diagnostic targets with different scales. Evaluation covers diagnostic reconstruction, voltage loss at individual current densities, aging-stage dependence, and the 30,000-cycle endpoint. Paired comparisons at the experimental-group level assess the effects of selected model components.

4. Results and discussion

4.1. Multi-diagnostic characteristics of electrochemical degradation

Electrochemical diagnostics revealed strong associations between cathode degradation and voltage loss under accelerated aging. At 30,000 cycles, electrochemically active surface area (ECSA) loss was strongly correlated with voltage loss at 1.0 A cm^{-2}, with a Spearman coefficient of 0.874 and a 95% bootstrap confidence interval (CI) of 0.772–0.942. The change in pressure-dependent oxygen-transport resistance showed a similarly strong correlation (Spearman = 0.847; 95% CI: 0.721–0.931). These results identify catalyst-surface deterioration and oxygen-transport changes as prominent experimental indicators of electrical performance degradation (Fig. 3a).

Other diagnostic quantities contributed complementary information. After controlling for ECSA loss through rank-residual analysis, changes in catalyst-layer ionic resistance (Rion) at 200 and 450 mV retained partial Spearman correlations of 0.655 and 0.637 with voltage loss at 1.0 A cm^{-2}, respectively. The corresponding partial correlations were 0.558 for pressure-dependent oxygen-transport resistance and −0.490 for high-frequency resistance (HFR) at 200 mV. These distinct associations, summarized in Fig. 3b, provide an experimental basis for representing catalyst/interface, protonic/ionic, ohmic, and mass-transport responses through separate diagnostic state groups.

ECSA evolution also exhibited nonmonotonic behavior during early aging. Five of the 37 experimental trajectories showed an ECSA increase exceeding 1% within the first 1000 cycles, while only 16 exhibited strictly monotonic ECSA decline across all measured stages. Figure 3c summarizes the prevalence of early ECSA increases and strictly monotonic decline among the 37 trajectories. The observed early activation and longer-term degradation motivate their separate representation in the catalyst-related state model.

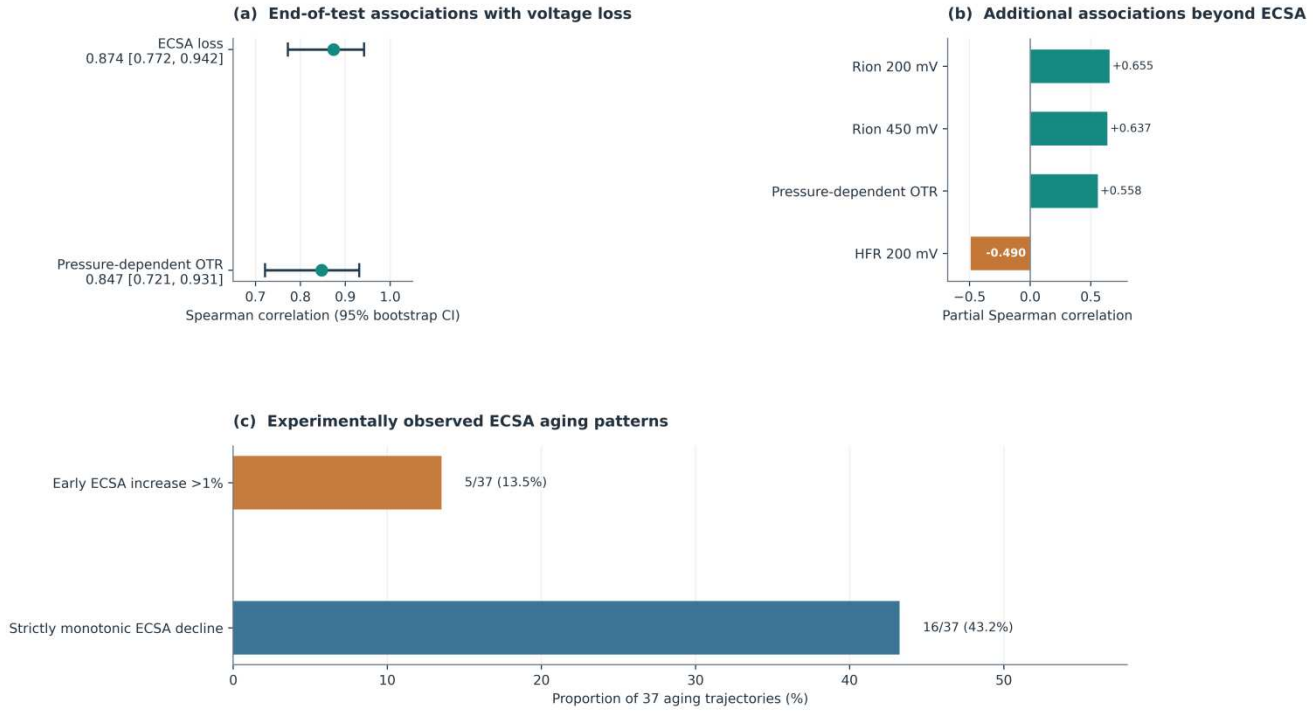


Figure 3. Reported electrochemical degradation associations and ECSA aging patterns. (a) Spearman correlations between end-of-test ECSA loss or pressure-dependent oxygen-transport resistance and voltage loss at 1.0 A cm^{-2}, with 95% bootstrap confidence intervals. (b) Partial Spearman correlations between other diagnostic changes and voltage loss after controlling for ECSA loss. (c) Fractions of the 37 aging trajectories showing an ECSA increase greater than 1% in the first 1000 cycles or strictly monotonic ECSA decline across measured stages. The displayed patterns do not encompass all trajectories.

4.2. Diagnostic fidelity of the learned degradation states

The diagnostic-anchored model reproduced multiple experimentally measured degradation responses in held-out cells. ECSA-loss reconstruction achieved $R^2 = 0.809$ and Spearman = 0.932. Stage-wise Spearman correlations reached 0.816, 0.874, and 0.880 at 1000, 10,000, and 30,000 cycles, respectively. The agreement across aging stages indicates that the catalyst-related representation captured both the temporal development and relative severity of active-area degradation. Figure 4a summarizes reconstruction R^2 for eight reported diagnostic targets, and Fig. 4b reports Spearman correlations for the targets with available rank statistics.

The remaining diagnostic groups provided additional measures of state fidelity. EIS-derived double-layer capacitance (Cdl) at 200 mV achieved $R^2 = 0.762$ and Spearman = 0.914. Rion reconstruction yielded R^2 values of 0.702 and 0.747 at 200 and 450 mV, respectively. The corresponding HFR reconstruction values were 0.743 and 0.643. These results demonstrate that the diagnostic observation branches retained measurable information about catalyst/interface, ionic, and ohmic changes.

Oxygen-transport reconstruction showed stronger agreement in degradation ranking than in magnitude. Each oxygen-transport-resistance target had 74 ensemble observations, compared with more than 320 for most CV- and EIS-derived targets. Pressure-dependent and pressure-independent transport-resistance changes achieved R^2 values of 0.172 and 0.100, respectively, with Spearman correlations of 0.662 and 0.605. The mass-transport coordinate therefore captured part of the relative variation among trajectories, while its quantitative reconstruction remained less accurate than that of the more frequently measured diagnostics.

At 30,000 cycles, ECSA-loss reconstruction yielded an MAE of 0.142 and a mean prediction bias of −0.097, with larger errors in severely degraded cells. Figure 4c shows ECSA-loss rank agreement at three aging stages alongside the reported endpoint MAE and bias. Together, the diagnostic results establish the ability of the learned representation to

reproduce major electrochemical aging trends, while identifying endpoint severity and sparse transport measurements as the principal sources of reconstruction uncertainty.

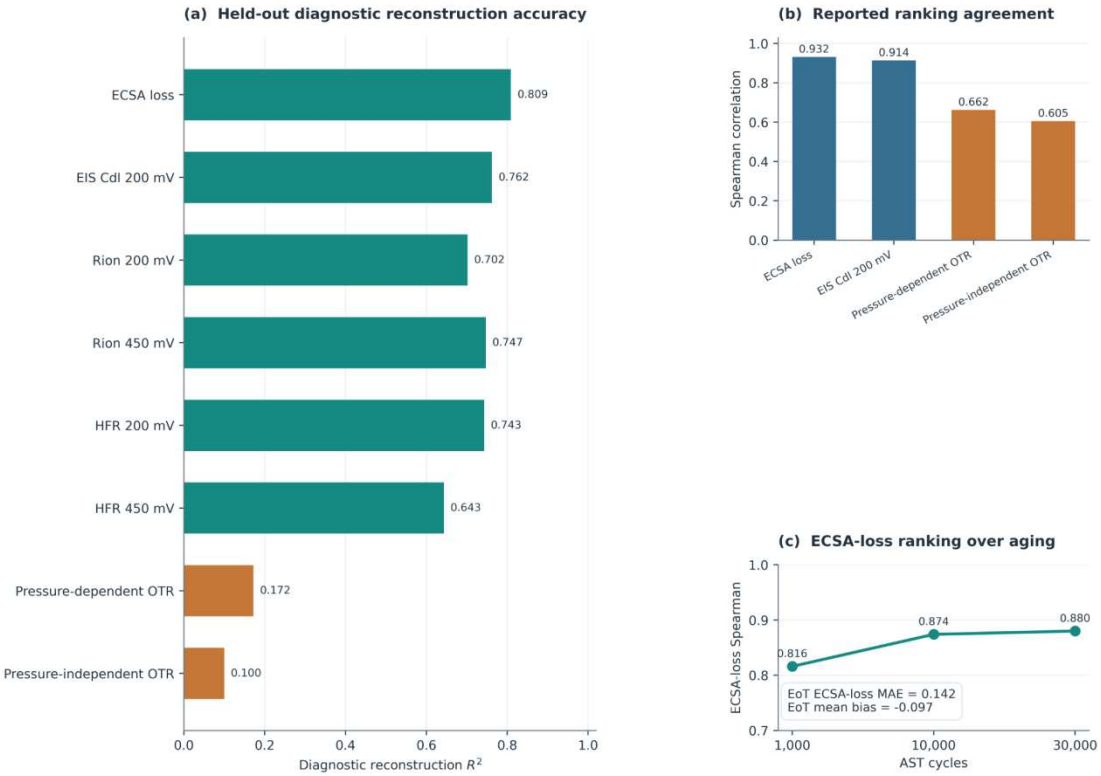


Figure 4. Summary of held-out electrochemical diagnostic reconstruction. (a) Coefficient of determination (R^2) for eight reported diagnostic targets, including ECSA, Cdl, Rion, HFR, and two oxygen-transport-resistance measures. (b) Spearman rank correlations for ECSA loss, EIS-derived Cdl at 200 mV, and pressure-dependent and pressure-independent oxygen-transport resistance. (c) ECSA-loss Spearman correlations at 1000, 10,000, and 30,000 AST cycles; the inset lists the separately evaluated end-of-test ECSA-loss MAE and mean prediction bias.

4.3. Cross-cell generalization of load-dependent voltage-loss prediction

The proposed EC-MP-NSSM achieved accurate voltage-loss prediction across five operating current densities under repeated cell-grouped fivefold cross-validation. The mean absolute error (MAE) across all five loads was 12.34 mV. The load-specific MAEs were 6.91, 11.70, 12.62, 13.56, and 16.89 mV at 0.1, 0.5, 1.0, 1.5, and 2.0 A cm^{-2}, respectively. At 1.0 A cm^{-2}, the model achieved $R^2 = 0.901$ and Spearman = 0.925. Prediction error increased with current density, consistent with the larger voltage-loss range and stronger high-load transport sensitivity.

Table 3 compares the proposed framework with regression, sequence-learning, and unconstrained state-space baselines evaluated using the same grouped protocol. Among the reported baselines, LSTM achieved the lowest mean MAE of 12.83 mV, followed by Transformer–GRU at 13.32 mV and GRU at 13.54 mV. The unconstrained neural state-space model yielded 14.36 mV. EC-MP-NSSM achieved the lowest reported mean MAE while additionally reconstructing electrochemical diagnostics through supervised state coordinates.

Table 3. Voltage-loss prediction performance of the proposed model and representative baselines under repeated physical-cell-grouped cross-validation.

Model	Mean MAE across five loads (mV)	MAE at 1.0 A cm^{-2} (mV)	R^2 at 1.0 A cm^{-2}
EC-MP-NSSM	12.34	12.62	0.901
LSTM	12.83	13.60	0.884
Transformer–GRU	13.32	14.12	0.893
GRU	13.54	14.31	0.866
Transformer	13.93	14.85	0.856
Unconstrained NSSM	14.36	15.22	0.853
TCN	14.78	16.02	0.872
Extra Trees	15.36	14.72	0.894
Random Forest	19.54	21.35	0.797

The difference between EC-MP-NSSM and LSTM was small at the physical-cell level. Their respective mean cell-level MAEs were 12.58 and 13.03 mV, and the paired Wilcoxon signed-rank test yielded p = 0.835. The comparison supports comparable predictive performance between these two models. The principal additional capability of EC-MP-NSSM is the joint representation of electrochemical diagnostic changes and load-dependent voltage loss.

Figure 5a compares mean voltage-loss MAE among the reported benchmark models, while Fig. 5b shows the EC-MP-NSSM prediction error across five operating current densities. The higher MAE at 2.0 A cm^{-2} indicates reduced prediction precision at the highest evaluated load; errors under severe degradation are analyzed in Section 4.7.

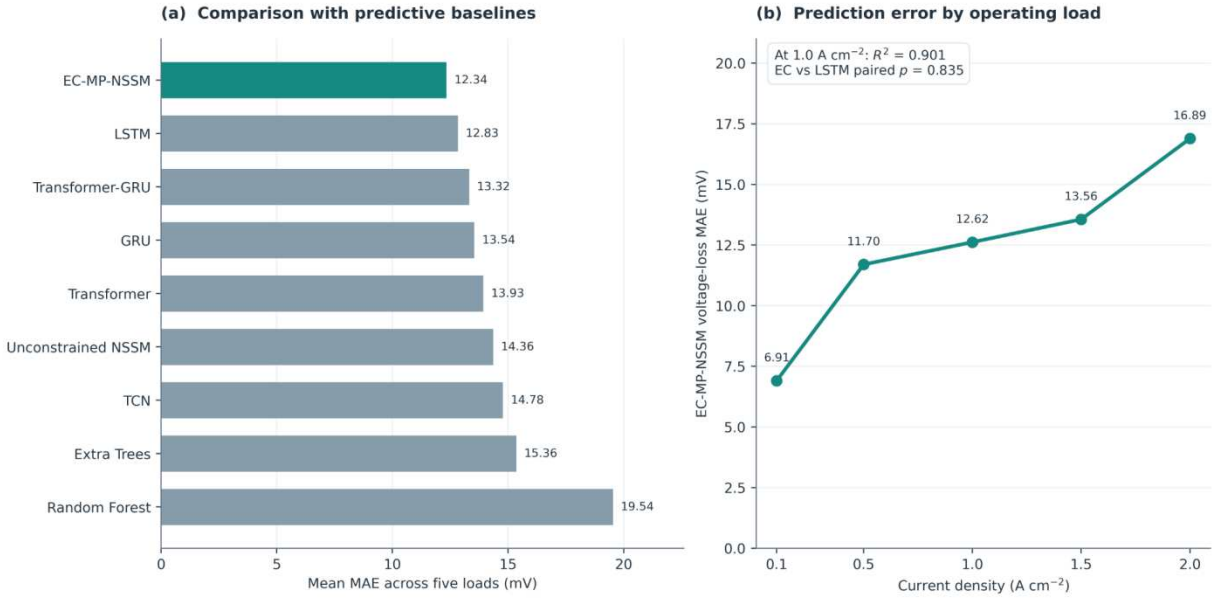


Figure 5. Summary of load-dependent voltage-loss prediction performance. (a) Mean MAE across five current densities for EC-MP-NSSM and the eight baselines reported in Table 3. (b) EC-MP-NSSM MAE at each of the five evaluated current densities. The annotation reports R^2 at 1.0 A cm^{-2} and the cell-level paired Wilcoxon p-value for the aggregate model comparison between EC-MP-NSSM and LSTM.

4.4. Material- and stress-dependent degradation-state evolution

Matched-condition comparisons revealed a consistent association between UPL and cathode degradation. Across 13 nominally matched pairs, increasing UPL from 0.95 to 1.15 V corresponded to median increases of 0.294 in end-of-test ECSA-loss fraction and 0.159 V in voltage loss at 1.0 A cm^{-2}. Both quantities increased under the higher UPL in all 13

comparisons. At 1.0 A cm^{-2}, the median additional voltage loss corresponds to a power-density penalty of 0.159 W cm^{-2}. Figure 6a and b summarize the median paired increases in ECSA loss and voltage loss, respectively, across the UPL, relative-humidity, and ionomer-to-carbon-ratio comparisons.

The conditioned catalyst-related state reproduced the observed UPL-dependent degradation ordering, and its diagnostic observation branch translated the state response into predicted ECSA loss. The agreement is consistent with the UPL-ordering constraint incorporated during training.

Additional matched comparisons indicated sensitivity to humidity and cathode composition. Across five matched pairs, increasing AST relative humidity from 40% to 100% corresponded to median increases of 0.323 in ECSA-loss fraction and 0.025 V in voltage loss at 1.0 A cm^{-2}. Across four pairs, increasing the ionomer-to-carbon ratio from 0.5 to 1.2 corresponded to median increases of 0.147 in ECSA-loss fraction and 0.038 V in voltage loss. These observations are consistent with experimentally established effects of ionomer composition and hydration on cathode aging[12,13]. The UPL comparison provides the largest matched sample among the reported contrasts and serves as the principal stress-dependent case study.

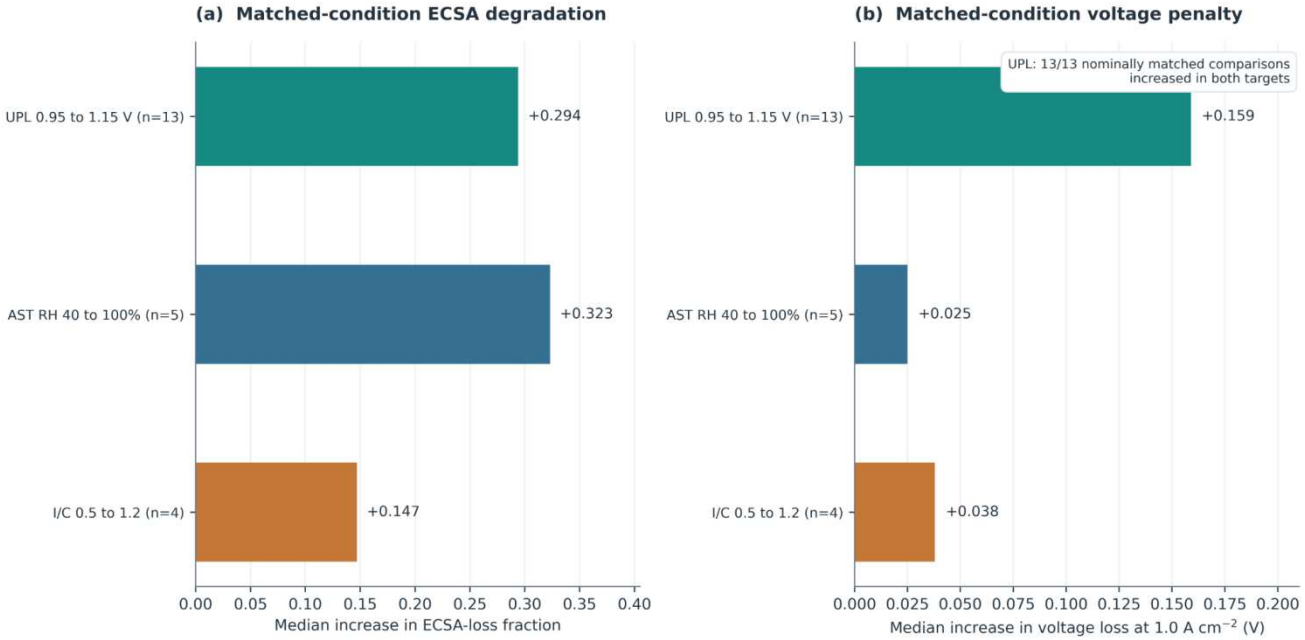


Figure 6. Summary of matched-condition differences in cathode degradation and voltage loss. (a) Median increases in end-of-test ECSA-loss fraction and (b) median increases in voltage loss at 1.0 A cm^{-2} for UPL (0.95 to 1.15 V; 13 matched comparisons), AST relative humidity (40% to 100%; five comparisons), and ionomer-to-carbon ratio (0.5 to 1.2; four comparisons). All 13 nominally matched UPL comparisons exhibited increases in both quantities. Bars show reported paired medians, not individual paired measurements or model predictions.

4.5. Load-dependent pathway contributions to voltage and power loss

The structured voltage decoder assigned different load sensitivities to the four explicit degradation pathways. At 30,000 cycles and 0.1 A cm^{-2}, the catalyst/interface term accounted for 97.4% of the mean normalized explicit-pathway contribution, whereas the mass-transport term contributed 1.2%. At 1.0 A cm^{-2}, the corresponding shares were 83.8% for catalyst/interface, 8.4% for mass transport, 4.6% for protonic/ionic response, and 3.2% for ohmic response.

At 2.0 A cm^{-2}, the catalyst/interface share decreased to 72.3%, while the mass-transport, protonic/ionic, and ohmic shares increased to 16.3%, 6.7%, and 4.7%, respectively. Figure 7a illustrates the reported contributions at three representative current densities (0.1, 1.0, and 2.0 A cm^{-2}). The increasing mass-transport share follows the nonlinear current dependence incorporated into the decoder and is consistent with the coupling between cathode aging and reactive transport described in

mechanistic studies[33–35].

The recurrent residual remained a substantial component of the modeled voltage response. Across the five loads, its median share of total decoder magnitude ranged from approximately 28.5% to 31.8%, reaching 28.5% at 2.0 A cm^{-2}. Figure 7b displays the reported range of median residual-magnitude fractions across the five loads, highlighting the value at 2.0 A cm^{-2}. The percentages in Fig. 7a are normalized over the four explicit pathway terms and exclude the residual; Fig. 7b reports the residual relative to the complete decoder magnitude. This distinction preserves the full modeled voltage-loss accounting and defines the reported contributions as model-attributed quantities.

Power-density loss follows directly from voltage-loss prediction through Eq. (2). At a fixed current density, multiplying each voltage contribution by current density preserves its normalized share while increasing its absolute power penalty. The model therefore connects load-sensitive degradation responses to their consequences for delivered electrical power.

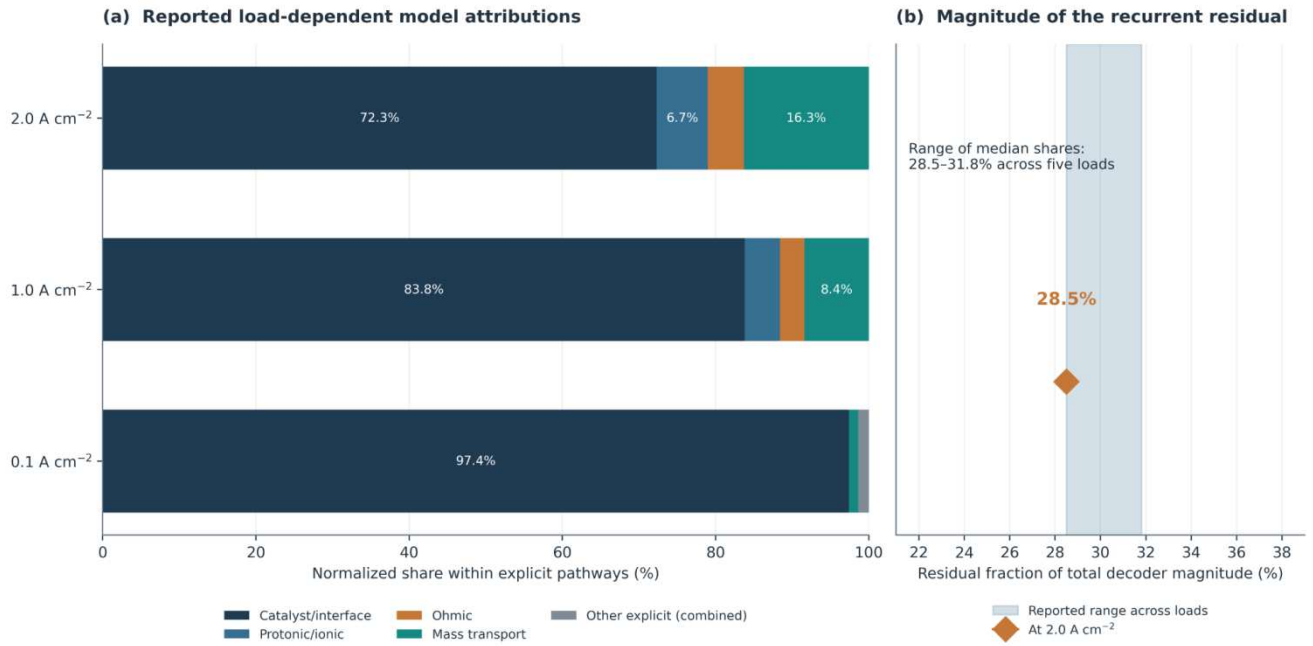


Figure 7. Reported model-attributed voltage-loss contributions at 30,000 AST cycles. (a) Normalized shares of the explicit catalyst/interface, protonic/ionic, ohmic, and mass-transport pathways at selected current densities (0.1, 1.0, and 2.0 A cm^{-2}). At 0.1 A cm^{-2}, the 1.4% remainder of the ionic and ohmic pathways is displayed as a combined segment because their individual shares were not reported. (b) Range of the median recurrent-residual magnitude fraction across five evaluated loads (28.5–31.8%), with the 2.0 A cm^{-2} value marked at 28.5%. The explicit-pathway percentages exclude the residual, which is normalized to the total decoder magnitude.

4.6. Ablation analysis of predictive and diagnostic model components

Ablation experiments were conducted to evaluate the contributions of individual model components to load-dependent voltage-loss prediction and electrochemical diagnostic reconstruction. As summarized in Table 4, the complete EC-MP-NSSM achieved the lowest mean voltage-loss MAE of 12.34 mV among all evaluated configurations. Removing material and stress conditioning produced the largest performance deterioration, increasing the mean MAE to 45.07 mV and reducing R^2 at 1.0 A cm^{-2} from 0.901 to −0.139. The difference was significant according to the paired Wilcoxon signed-rank test at the physical-cell level ($p = 1.16 \times 10^{-6}$). These results highlight the importance of cathode formulation and accelerated-stress descriptors for distinguishing degradation behavior across experimental trajectories.

The structured voltage decoder and recurrent residual correction also contributed to predictive accuracy. Replacing the structured decoder with an unconstrained mapping increased the mean MAE from 12.34 to 15.50 mV ($p = 0.018$), while

removing the residual correction increased it to 14.83 mV ($p = 0.015$). These results support the use of pathway-specific load-response functions to represent the current dependence of voltage loss, together with a residual component that accommodates behavior not fully captured by the explicit diagnostic pathways.

Table 4. Voltage-loss prediction performance of the complete model and targeted ablations.

Model configuration	Mean MAE across five loads (mV)
Complete EC-MP-NSSM	12.34
Without material/stress conditioning	45.07
Without structured voltage decoder	15.50
Without residual correction	14.83
Without mass-transport-to-voltage contribution	13.14
Without transient activation	13.56
Without complete physics penalty	12.72
Without UPL-ordering constraint	13.79

The remaining electrochemical components provided additional improvements of varying magnitude. Removing the explicit mass-transport-to-voltage contribution increased the mean MAE to 13.14 mV, while excluding transient catalyst activation increased it to 13.56 mV. Removing the complete set of electrochemically motivated penalties resulted in an MAE of 12.72 mV, whereas excluding the UPL-ordering constraint increased the error to 13.79 mV. Although these changes were smaller than those associated with removing material and stress conditioning or the structured decoder, all evaluated ablations produced higher voltage-prediction errors than the complete model. The comparatively small change following removal of the electrochemical penalties indicates that their additional contribution to aggregate voltage accuracy was modest under the investigated conditions.

Transient catalyst activation also contributed to electrochemical diagnostic reconstruction. In the transient-activation ablation, its removal increased the reported ECSA-loss reconstruction MAE from approximately 0.094 to 0.110, alongside increased voltage-loss prediction error. The endpoint-specific ECSA-loss MAE of 0.142 is reported separately in Section 4.2. This result supports the inclusion of a transient activation response to accommodate the early ECSA increases observed in some experimental trajectories. The explicit mass-transport contribution and UPL-ordering constraint likewise improved aggregate voltage prediction, although their effects should be interpreted within the model structure and the investigated accelerated-stress conditions.

Taken together, the ablation results indicate that material and stress conditioning, load-structured voltage decoding, and recurrent residual correction are the principal contributors to predictive performance. Transient activation and electrochemically motivated constraints provide further improvements, while supporting the diagnostic-oriented structure of the framework. The complete model therefore offers the best aggregate voltage-prediction accuracy among the evaluated configurations while retaining the ability to reconstruct multiple electrochemical degradation responses.

4.7. Applicability and limitations

The results establish the applicability of diagnostic-anchored state-space modeling to comparative PEMFC cathode durability assessment within the investigated material and accelerated-stress conditions. The framework reproduced major electrochemical degradation trends, predicted voltage loss across five loads in held-out cells, and linked material and stress descriptors to the evolution of diagnostic states.

Prediction accuracy decreased for severely degraded observations. At 1.0 A cm^{-2}, voltage-loss observations above 0.2 V exhibited a mean prediction bias of approximately −35.0 mV, increasing in magnitude to −51.5 mV for observations above 0.3 V. ECSA reconstruction also underestimated some high-loss endpoints. These results identify severe degradation as the principal region requiring improved predictive calibration.

Oxygen-transport diagnostics were concentrated near the beginning and end of testing, limiting the quantitative resolution of the mass-transport state. The current validation also focuses on cathode-oriented accelerated voltage cycling.

Application to other membrane-electrode assemblies, material systems, or operational stress histories will require evaluation under the corresponding experimental conditions. Within the studied domain, the framework provides a common basis for connecting electrochemical degradation measurements with load-dependent electrical performance.

5. Conclusions

This study developed a diagnostic-anchored neural state-space framework linking electrochemical degradation to load-dependent voltage loss in proton exchange membrane fuel cells. Four evolving state coordinates were supervised by ten electrochemical diagnostic targets representing catalyst/interface, protonic/ionic, ohmic, and oxygen-transport responses. Material and stress descriptors conditioned state evolution, while measurement-availability masks accommodated diagnostics collected at different aging stages. A load-structured decoder connected the evolving states to voltage and power-density losses across five current densities, enabling joint assessment of electrochemical degradation and electrical performance.

Across 37 curated aging trajectories, repeated cell-grouped fivefold cross-validation yielded a mean voltage-loss MAE of 12.34 mV, with $R^2 = 0.901$ at 1.0 A cm^{-2}. ECSA-loss reconstruction achieved $R^2 = 0.809$, demonstrating the model's ability to reproduce experimentally measured catalyst-related degradation. Replacing the structured voltage decoder increased mean MAE to 15.50 mV, while removing material and stress conditioning increased it to 45.07 mV. In 13 nominally matched comparisons, increasing the upper potential limit from 0.95 to 1.15 V was associated with median increases of 0.294 in ECSA-loss fraction and 0.159 V in voltage loss at 1.0 A cm^{-2}. These findings establish the combined predictive and diagnostic capabilities of the proposed framework.

The framework provides a unified approach for relating cathode formulation, accelerated-stress conditions, electrochemical degradation, and load-dependent performance loss. Its application to comparative cathode durability assessment is supported within the investigated experimental domain. Further improvements in severe-degradation prediction and sparsely sampled oxygen-transport reconstruction would strengthen its quantitative reliability.

References

1. International Energy Agency. *Global Hydrogen Review 2026*. https://www.iea.org/reports/global-hydrogen-review-2026 (IEA, Paris, 2026).
2. European Parliament and Council of the European Union. Regulation (EU) 2023/1804 on the deployment of alternative fuels infrastructure. *Off. J. Eur. Union* **L 234,** 1–47 (2023). https://eur-lex.europa.eu/eli/reg/2023/1804/oj/eng.
3. U.S. Department of Energy. *The Department of Energy Hydrogen Program Plan*. https://www.hydrogen.energy.gov/library/roadmaps-vision/program-plan (U.S. Department of Energy, Washington, DC, 2024).
4. Mdlovu, N. V. et al. Hydrogen production enhancement via methanol steam reforming with copper-zinc catalysts. *J. Energy Inst.* **122,** 102203 (2025). https://doi.org/10.1016/j.joei.2025.102203.
5. Cullen, D. A. et al. New roads and challenges for fuel cells in heavy-duty transportation. *Nat. Energy* **6,** 462–474 (2021). https://doi.org/10.1038/s41560-021-00775-z.
6. Mora, D. et al. Impact of cell temperature on cathode catalyst layer oxygen transport resistance and performance ageing under heavy-duty conditions. *J. Power Sources* **677,** 239992 (2026). https://doi.org/10.1016/j.jpowsour.2026.239992.
7. El-Kharouf, A., Chandan, A., Hattenberger, M. & Pollet, B. G. Proton exchange membrane fuel cell degradation and testing: review. *J. Energy Inst.* **85,** 188–200 (2012). https://doi.org/10.1179/1743967112Z.00000000036.
8. Borup, R. et al. Scientific aspects of polymer electrolyte fuel cell durability and degradation. *Chem. Rev.* **107,** 3904–3951 (2007). https://doi.org/10.1021/cr0501821.
9. Laghryb, I., Malki, M., Yousfi Steiner, N., Barrett, C. D. & El Kadiri, H. Catalyst degradation in proton exchange membrane fuel cells: mechanisms, investigation techniques, and predictive modelling. *Int. J. Hydrogen Energy* **145,** 496–507 (2025). https://doi.org/10.1016/j.ijhydene.2025.06.052.
10. Coats, M. T. & Pylypenko, S. Cathode catalyst layer degradation in proton exchange membrane fuel cells under idle and load cycling conditions. *ACS Appl. Energy Mater.* **8,** 14919–14946 (2025). https://doi.org/10.1021/acsaem.5c01392.
11. Lim, K. H. et al. Transfer-enhanced cathode with noncorrosive inorganic-based composite additive for durable proton exchange membrane fuel cells. *J. Power Sources* **644,** 237063 (2025). https://doi.org/10.1016/j.jpowsour.2025.237063.
12. Schneider, P. et al. The effect of ionomer to carbon ratio and relative humidity on cathode catalyst degradation in PEM fuel cells. *J. Electrochem. Soc.* **170,** 104505 (2023). https://doi.org/10.1149/1945-7111/acff1f.
13. Pedram, S. et al. Data-driven quantitative microscopy to explain ionomer–carbon ratio and humidity effects on cathode structure–performance degradation in proton exchange membrane fuel cells. *J. Power Sources* **677,** 240009 (2026). https://doi.org/10.1016/j.jpowsour.2026.240009.

14. Zheng, T. et al. Diagnosis of ionomers degradation in proton-exchange membrane fuel cell. *J. Power Sources* **647,** 237303 (2025). https://doi.org/10.1016/j.jpowsour.2025.237303.
15. Jeong, E., Park, J., Lee, S. H. & Litster, S. E. Chemical degradation of ionomer in the electrodes of proton exchange membrane fuel cells. *J. Power Sources* **657,** 238160 (2025). https://doi.org/10.1016/j.jpowsour.2025.238160.
16. Raab, S. & Weber, A. Impedance-based analysis of PEMFC degradation phenomena during accelerated stress tests. *J. Power Sources* **673,** 239725 (2026). https://doi.org/10.1016/j.jpowsour.2026.239725.
17. García-Salaberri, P. A., Das, P. K. & Chaparro, A. M. Local oxygen transport resistance in polymer electrolyte fuel cells: origin, dependencies and mitigation. *Front. Energy Res.* **12,** 1357325 (2024). https://doi.org/10.3389/fenrg.2024.1357325.
18. Afra, M., Klütsch, J., Özyalcin, C., Fleming, J. & Curnick, O. In-situ measurements of oxygen concentration at the PEMFC cathode catalyst layer/membrane interface. *J. Power Sources* **658,** 238275 (2025). https://doi.org/10.1016/j.jpowsour.2025.238275.
19. Aslam, R. M. et al. Simultaneous thermal and visual imaging of liquid water of the PEM fuel cell flow channels. *J. Energy Inst.* **92,** 311–318 (2019). https://doi.org/10.1016/j.joei.2018.01.005.
20. Schneider, P. et al. In-situ characterization of cathode catalyst degradation in PEM fuel cells. *Sci. Data* **11,** 828 (2024). https://doi.org/10.1038/s41597-024-03662-w.
21. Ma, Y. et al. Data-driven electrochemically active surface area loss modeling and its application in fuel cell stack degradation prediction. *J. Power Sources* **659,** 238354 (2025). https://doi.org/10.1016/j.jpowsour.2025.238354.
22. Dong, Y. et al. An improved data-driven approach and a voltage integral indicator for remaining useful life estimation of proton exchange membrane fuel cells. *J. Power Sources* **640,** 236726 (2025). https://doi.org/10.1016/j.jpowsour.2025.236726.
23. Hua, Z. et al. Degradation prediction of hydrogen fuel cell based on dynamic comprehensive aging indicator and hybrid forecasting method. *J. Power Sources* **642,** 236914 (2025). https://doi.org/10.1016/j.jpowsour.2025.236914.
24. Quan, R., Cheng, G., Guan, X., Zhang, G. & Quan, J. A HO-BiGRU-Transformer based PEMFC degradation prediction method under different current conditions. *Renew. Energy* **256,** 124132 (2026). https://doi.org/10.1016/j.renene.2025.124132.
25. Yu, Y. et al. Degradation and polarization curve prediction of proton exchange membrane fuel cells: an interpretable model perspective. *Appl. Energy* **365,** 123289 (2024). https://doi.org/10.1016/j.apenergy.2024.123289.
26. Zhang, Z. et al. A novel generalized prognostic method of proton exchange membrane fuel cell using multi-point estimation under various operating conditions. *Appl. Energy* **357,** 122519 (2024). https://doi.org/10.1016/j.apenergy.2023.122519.
27. Ke, C., Han, K. & Wang, Y. A hybrid method combining degradation mechanisms and deep learning for lifetime prediction of proton exchange membrane fuel cells under dynamic load cycle conditions. *J. Power Sources* **633,** 236464 (2025). https://doi.org/10.1016/j.jpowsour.2025.236464.
28. Guo, B. et al. An interpretable uncertainty quantification framework for proton exchange membrane fuel cell degradation prediction. *Renew. Energy* **249,** 123137 (2025). https://doi.org/10.1016/j.renene.2025.123137.
29. Ko, T., Kim, D., Park, J. & Lee, S. H. Physics-informed neural network for long-term prognostics of proton exchange membrane fuel cells. *Appl. Energy* **382,** 125318 (2025). https://doi.org/10.1016/j.apenergy.2025.125318.
30. Wei, L., Gao, S., Chen, Z., Wang, Y. & Sun, Z. A hybrid framework for PEMFC degradation prediction integrating Crossformer and physical constraints. *J. Power Sources* **677,** 239941 (2026). https://doi.org/10.1016/j.jpowsour.2026.239941.
31. Liu, M., Yang, Y., Cheng, J., Cui, J. & Zheng, X. Credible long-term degradation prediction for proton exchange membrane fuel cell: a physics-informed neural network with conformal prediction approach. *Reliab. Eng. Syst. Saf.* **276,** 112945 (2026). https://doi.org/10.1016/j.ress.2026.112945.
32. Zhu, W., Xu, B., Guo, B., Xie, C. & Xiong, R. Data-efficient and interpretable long-term prognostics of PEMFC degradation via physics-constrained symbolic regression–physics-informed neural network. *eTransportation* **29,** 100615 (2026). https://doi.org/10.1016/j.etran.2026.100615.
33. Hao, M., Hu, Y., Chen, S. & Li, Y. A scale-bridging model for proton exchange membrane fuel cells: understanding interactions among multi-physics transports, electrochemical reactions and heterogeneous aging. *Nano Energy* **128,** 109957 (2024). https://doi.org/10.1016/j.nanoen.2024.109957.
34. Goswami, N., Grunewald, J. B., Fuller, T. F. & Mukherjee, P. P. Probing multiphase reactive transport interactions in the polymer electrolyte fuel cell catalyst layer degradation. *Electrochim. Acta* **486,** 144143 (2024). https://doi.org/10.1016/j.electacta.2024.144143.
35. Liu, F., Jiang, J., Ji, X., Guo, L. & Su, J. Carbon corrosion in PEMFCs: mechanistic insight into the cause of mass transport degradation and its nonlinear behavior. *Electrochim. Acta* **548,** 147850 (2026). https://doi.org/10.1016/j.electacta.2025.147850.
36. Schneider, P. et al. In-Situ Characterization of Cathode Catalyst Degradation in PEM Fuel Cells. *figshare* https://doi.org/10.6084/m9.figshare.25450177 (2024).